

## APPLIED SCIENCES AND ENGINEERING

## A highly stretchable, transparent, and conductive polymer

Yue Wang,<sup>1</sup> Chenxin Zhu,<sup>2</sup> Raphael Pfattner,<sup>1</sup> Hongping Yan,<sup>3</sup> Lihua Jin,<sup>1,4</sup> Shucheng Chen,<sup>1</sup> Francisco Molina-Lopez,<sup>1</sup> Franziska Lissel,<sup>1</sup> Jia Liu,<sup>1</sup> Noelle I. Rabiah,<sup>1</sup> Zheng Chen,<sup>1</sup> Jong Won Chung,<sup>1,5</sup> Christian Linder,<sup>4</sup> Michael F. Toney,<sup>3</sup> Boris Murmann,<sup>2</sup> Zhenan Bao<sup>1\*</sup>

2017 © The Authors,  
some rights reserved;  
exclusive licensee  
American Association  
for the Advancement  
of Science. Distributed  
under a Creative  
Commons Attribution  
NonCommercial  
License 4.0 (CC BY-NC).

Previous breakthroughs in stretchable electronics stem from strain engineering and nanocomposite approaches. Routes toward intrinsically stretchable molecular materials remain scarce but, if successful, will enable simpler fabrication processes, such as direct printing and coating, mechanically robust devices, and more intimate contact with objects. We report a highly stretchable conducting polymer, realized with a range of enhancers that serve a dual function: (i) they change morphology and (ii) they act as conductivity-enhancing dopants in poly(3,4-ethylenedioxythiophene):poly(styrenesulfonate) (PEDOT:PSS). The polymer films exhibit conductivities comparable to the best reported values for PEDOT:PSS, with over 3100 S/cm under 0% strain and over 4100 S/cm under 100% strain—among the highest for reported stretchable conductors. It is highly durable under cyclic loading, with the conductivity maintained at 3600 S/cm even after 1000 cycles to 100% strain. The conductivity remained above 100 S/cm under 600% strain, with a fracture strain of 800%, which is superior to even the best silver nanowire- or carbon nanotube-based stretchable conductor films. The combination of excellent electrical and mechanical properties allowed it to serve as interconnects for field-effect transistor arrays with a device density that is five times higher than typical lithographically patterned wavy interconnects.

## INTRODUCTION

Recent advancements in stretchable electronics have blurred the interfaces between human and machine (1, 2). Devices such as epidermal electronics, implantable sensors, and hemispherical eye cameras all rely on the intimate contact between devices and curvilinear surfaces of various biological systems while operating with stability under up to 100% strain (3–5). The most successful concept leading to such devices builds on linking rigid islands of active components [that is, transistors, light-emitting diodes (LEDs), or photovoltaics] with stretchable interconnects (1, 3, 6, 7). Hence, developing conductors that can retain good electrical performance under high mechanical strain is paramount.

Stretchable conductors have been fabricated via two main routes: strain engineering and nanocomposites (1, 8, 9). In the first approach, nonstretchable inorganic materials, such as metals, are geometrically patterned into wavy lines that can be extended when the underneath elastomer substrate is stretched (10). Alternatively, depositing a thin layer of conducting materials such as metals, carbon nanotubes, or graphene on a prestrained substrate leads to the formation of periodic buckles upon the release of the strain, which allows the material to accommodate further cycles of stretching up to the initial prestrained value (5). A kirigami design or microcracks have also been applied to sheets of flexible materials to enable macroscopic stretching motion (11–13). These methods demonstrate the possibility of transforming virtually any rigid materials into stretchable materials while maintaining their electrical properties. However, the fabrication methods involved are usually complicated, and it is challenging to achieve high device density owing to the large geometric patterns required for high stretchability. In addition, the buckling and kirigami methods lead to out-of-plane patterns, which

could be difficult to encapsulate and disadvantageous for devices that require planar interfaces or lower profiles.

Embedding a conductive filler in an insulating elastomeric matrix to form a nanocomposite is the second major route toward stretchable conductors (8, 14). Typically, one-dimensional materials such as carbon nanotubes (CNTs) and silver nanowires are chosen as the conductive fillers because of their high aspect ratios (15–17). Metal nanoparticles or flakes have also been shown to be good filler materials under specific conditions because of their ability to self-organize upon stretching (7, 18). Despite the versatility and large number of material choices, the percolation-dependent conductivity is highly strain-sensitive and remains a hurdle for device miniaturization and cycling stability (8).

To achieve a highly stretchable and highly conductive material that is readily solution-processable and patternable, an intrinsically stretchable conductor is desirable. Conducting polymers are good candidates because of the flexibility in tuning the molecular structures and electrical and mechanical properties. Their solution processability offers additional advantages for large-scale production of flexible electronics. Unfortunately, high conductivity and high stretchability have not been achieved simultaneously for conducting polymers (19–21).

In general, to achieve high conductivity, high crystallinity and low insulating content are required. However, to render a polymer film stretchable, a high degree of disorder with chain folding is advantageous to create a large free volume for polymer chain movement and unfolding when being stretched (22, 23). Poly(3,4-ethylenedioxythiophene):poly(styrenesulfonate) (PEDOT:PSS) has the highest reported conductivity among solution-processed polymers but has a fracture strain of as low as ~5% (20). Previous efforts enabled the stretching of PEDOT:PSS by incorporating plasticizers such as Zonyl or Triton (19–21). However, the enhanced stretchability often results in much lower conductivities, and the value further decreases with the application of strain. As yet, the best reported value is 550 S/cm under 0% strain and a conductivity of 13 S/cm under a fracture strain of 188% (20). Hence, these materials have generally been used as pressure or strain sensors where a large change in electrical signal upon strain is desirable, but they fail to serve as interconnects.

<sup>1</sup>Department of Chemical Engineering, Stanford University, Stanford, CA 94305, USA.

<sup>2</sup>Department of Electrical Engineering, Stanford University, Stanford, CA 94305, USA.

<sup>3</sup>Stanford Synchrotron Radiation Lightsource, SLAC National Accelerator Laboratory, Menlo Park, CA 94025, USA. <sup>4</sup>Department of Civil and Environmental Engineering, Stanford University, Stanford, CA 94305, USA. <sup>5</sup>Samsung Advanced Institute of Technology, Yeongtong-gu, Suwon-si, Gyeonggi-do 443-803, South Korea.

\*Corresponding author. Email: zbao@stanford.edu

Interconnects for various rigid electrical components in circuits require an intrinsically stretchable conducting polymer with conductivity  $>1000$  S/cm at  $>100\%$  strain and minimal temperature dependence.

Here, we demonstrate a method for creating highly stretchable and conductive PEDOT films with high cycling stability by incorporating ionic additives–assisted stretchability and electrical conductivity (STEC) enhancers (Fig. 1, A and B). The resulting PEDOT:PSS films are both highly conductive and stretchable (higher than 4100 S/cm under 100% strain), giving rise to transistor arrays up to five times higher in island-to-interconnect ratio as compared to those using wavy metal interconnects.

## RESULTS

### Selection of STEC enhancers

We rationalized that high stretchability requires polymer films with both hard and soft domains, typically seen with hydrogenated styrene ethylene butylene styrene (SEBS) block copolymers or polyurethane elastomers (23). Unfortunately, both PEDOT and PSS are semicrystalline polymers with no observable glass transition temperatures (24). Therefore, the STEC enhancers need to partially soften polymer chains to create soft domains in order to achieve high fracture strain. To promote high conductivity, it is important to have good connectivity between PEDOT-rich domains, which requires a weakened electrostatic

interaction between PEDOT and PSS to allow PEDOT to partially aggregate to form a “hard” conductive network inside a soft PSS matrix (Fig. 1D). Previous studies reported various additives used to promote some of the effects (20, 21, 25). However, either solely improved conductivity or solely improved stretchability was reported. Here, we introduce a new approach, in which STEC enhancers soften the PSS domains and promote better connectivity and higher crystallinity in PEDOT regions while further enhancing electrical conductivity through doping.

We identified a number of effective STEC enhancers, including ionic compounds such as dioctyl sulfosuccinate sodium salt, sodium dodecylbenzenesulfonate, dodecylbenzenesulfonic acid, and ionic liquids (table S1 and fig. S1). All these molecules have sulfonate or sulfonimide anions, which are effective dopants for conducting polymers, including PEDOT (26). We focus our study on the ionic liquids because of the large number of commercially available varieties. These compounds not only effectively reduce Young’s moduli of PEDOT:PSS bulk film by as much as 50 times and render it highly extensible, but also preserve or increase the conductivity (table S1 and fig. S1).

We found that a synergistic effect on both conductivity and stretchability can be achieved when the STEC enhancers satisfy the following two characteristics: (i) good solubility in water and the PEDOT:PSS matrix and (ii) highly acidic anions that can act as effective dopants

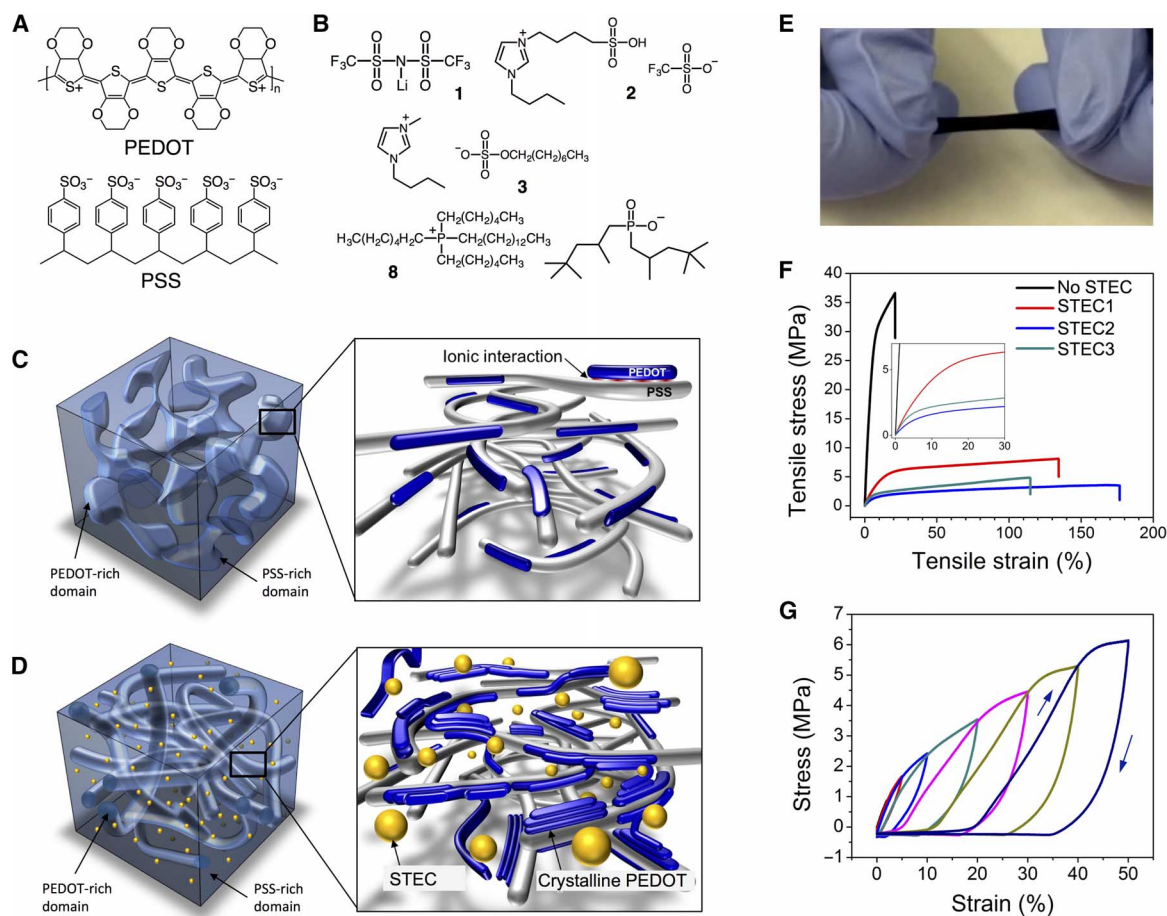


**Fig. 1. Chemical structures and schematic representation.** (A and B) Chemical structures of PEDOT:PSS (A) and representative STEC enhancers (B) (see complete list in the Supplementary Materials). (C and D) Schematic diagram representing the morphology of a typical PEDOT:PSS film (C) versus that of a stretchable PEDOT film with STEC enhancers (D). (E) Photograph showing a freestanding PEDOT/STEC film being stretched. (F and G) Stress/strain (F) and strain cycling behavior (G) of freestanding PEDOT/STEC films.

for PEDOT. Through the evaluation of electrical and mechanical properties of freestanding PEDOT/STEC films, we found that STEC enhancers 1 to 3 (Fig. 1A) lead to both high conductivity and good stretchability (Fig. 1, E and F, and sections S1 and S2). Even with as high as 40 to 50 weight % (wt %) incorporation of STEC enhancers, the rheological characteristics of the bulk films are similar to those of viscoelastic solids (Fig. 1G and sections S1 and S2). Therefore, we chose these systems for further investigations.

### Highly conductive and stretchable PEDOT film supported on elastic substrates

Stretchable PEDOT is characterized using thin films directly coated onto SEBS elastic substrates to evaluate their electrical behavior as transparent, thin-film electronic components. When stretched, an initial increase in conductivity by almost three times to up to 3390 S/cm under 100% strain was observed along the stretching direction ( $\sigma_{\parallel}$ ), but it de-

creased in the perpendicular direction ( $\sigma_{\perp}$ ) (Fig. 2, A and B). A high degree of PEDOT chain alignment was confirmed by polarized ultraviolet-visible (UV-vis) measurement (Fig. 2G). The dichroic ratios ( $A_{\parallel}/A_{\perp}$ ) calculated using the absorption of the 785-nm peak and the free-carrier tail at 1100 nm both showed a monotonic increase from 1 under 0% strain to  $\sim 3.2$  under 125% strain, which is indicative of chain alignment along the parallel direction to stretching (Fig. 2G). This agrees with the increase in conductivity along this direction (Fig. 2A).

Followed by the initial increase at lower strains,  $\sigma_{\parallel}$  then decreased consistently under  $>100\%$  strain until the substrate ruptured. We obtained the best performance for films with STEC enhancer 1, where the conductivity remained above 1000 S/cm between 0 and 100% strain, with the highest value at 3390 S/cm under 100% strain, above 100 S/cm up to 600% strain, and a final conductivity of 56 S/cm even when stretched to a record 800% strain, beyond which point the substrate ruptured. Optical microscope images of the stretchable PEDOT films

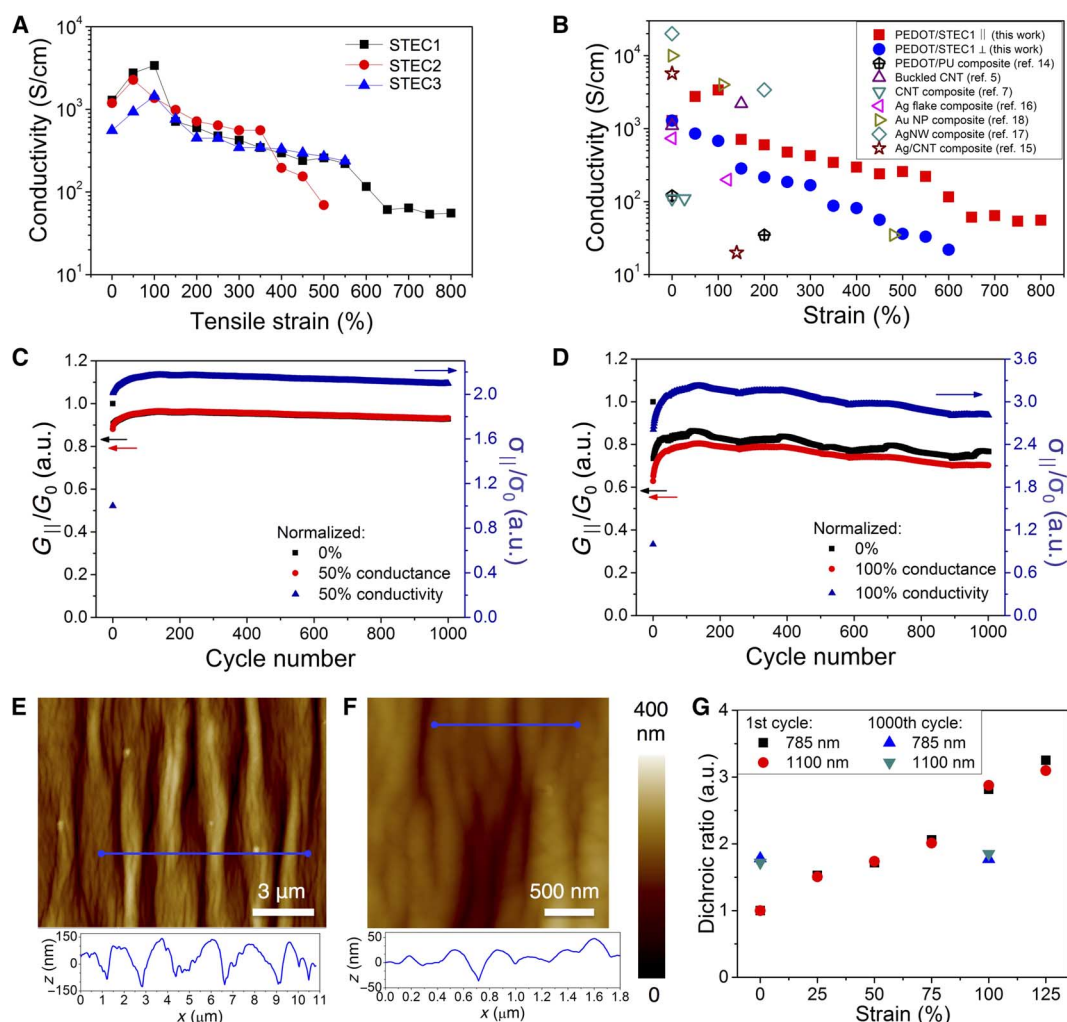


**Fig. 2. Electrical and optical properties of stretchable PEDOT under strain.** (A) Conductivity under various strains for PEDOT with different STEC enhancers. Film thicknesses are around 600 to 800 nm. (B) Conductivities under various strain presented in this work compared to representative stretchable conductors reported in literature. PU, polyurethane. (C and D) Cycling stability of PEDOT/STEC1 under 50% strain (C) and 100% strain (D).  $G$ , conductance;  $\sigma$ , conductivity; a.u., arbitrary units. (E and F) AFM images of a PEDOT/STEC1 film under different magnifications under 0% strain after it was cycled for 1000 times to 100% strain. The vertical profile across the line on the image is shown below the corresponding image. The deep folds have an amplitude of  $\sim 100$  nm and a periodicity of  $\sim 1.5$   $\mu\text{m}$ , whereas those for the wrinkles are  $\sim 20$  nm and  $\sim 0.25$   $\mu\text{m}$ , respectively. (G) Dichroic ratio of the PEDOT/STEC1 films under different strains calculated at 785 and 1100 nm for the 1st and the 1000th cycle. There is no change in dichroic ratio from 0 to 100% strain after 1000 cycles, potentially because of the folds formed in the film and a steady concentration of STEC enhancers being reached.



held under strain show that cracks do not form until ~150% (section S5). Even under strains as high as 550% with a much higher crack density, the films have morphologies of an interconnected network, which could account for the reasonably high conductivity under high strain. Compared to most reported stretchable conductors (Fig. 2B), our material not only has a higher initial conductivity and a slower drop in conductivity under tensile strain but also sustains the highest maximum tensile strain. Note that, although a maximum 100% strain is necessary for wearable or epidermal electronics, a higher stretchability is required when these materials are used as interconnects for rigid-island device arrays shown later. In addition, the ability for a material to be elongated to several times its original length greatly broadens its applications to robotics and biomechanical systems under extreme conditions.

The stretchable PEDOT films show high cycling stability. The film conductance  $G$  (reflects change in resistance) retained 92% of the original value under 50% strain after 1000 cycles and 71% when the cycling strain was 100% (Fig. 2, C and D). The conductivity ( $\sigma_{||}$ ) of these films increased with strain as a result of the chain alignment phenomenon. After 1000 cycles, the films still exhibited a 2.1- and 2.8-fold increase in conductivity under 50 and 100% strains, respectively, as compared to the unstrained films (Fig. 2, C and D). Note that the conductivity ex-

hibited an increase during approximately the first 100 cycles but then stabilized at a more constant value. At the end of 1000 cycles to 100% strain, no visible cracks formed on films when inspected under an optical microscope (section S4) and an atomic force microscope (AFM) (Fig. 2, E and F). The darker lines visible in optical microscope images were revealed to be deep folds by AFM analysis (Fig. 2, E and F), demonstrating the excellent durability of the PEDOT/STEC films under repeated strain.

### Stretchable PEDOT film morphological characterizations

We found that the STEC enhancers (such as 1 to 3) play a number of roles in PEDOT:PSS in terms of charge transfer doping, crystallinity, and morphology. First, it has been documented that small ionic species can have a charge screening effect that weakens the Coulombic interactions between the polyelectrolytes PEDOT and PSS (25, 27–29). The charge screening effect was previously found to result in higher crystallinity of the PEDOT-rich domains (25, 28). We observed larger colloidal particle sizes in solution with the addition of STEC by dynamic light scattering analysis (fig. S3, B and C). In addition, more distinct nanofibrous structures were seen in dried films by AFM (Fig. 3, H to K, and fig. S4). In thin films, we observed that  $C_{\alpha}=C_{\beta}$  vibration peaks ( $\sim 1445\text{ cm}^{-1}$ ) in Raman spectroscopy red-shifted and were narrower

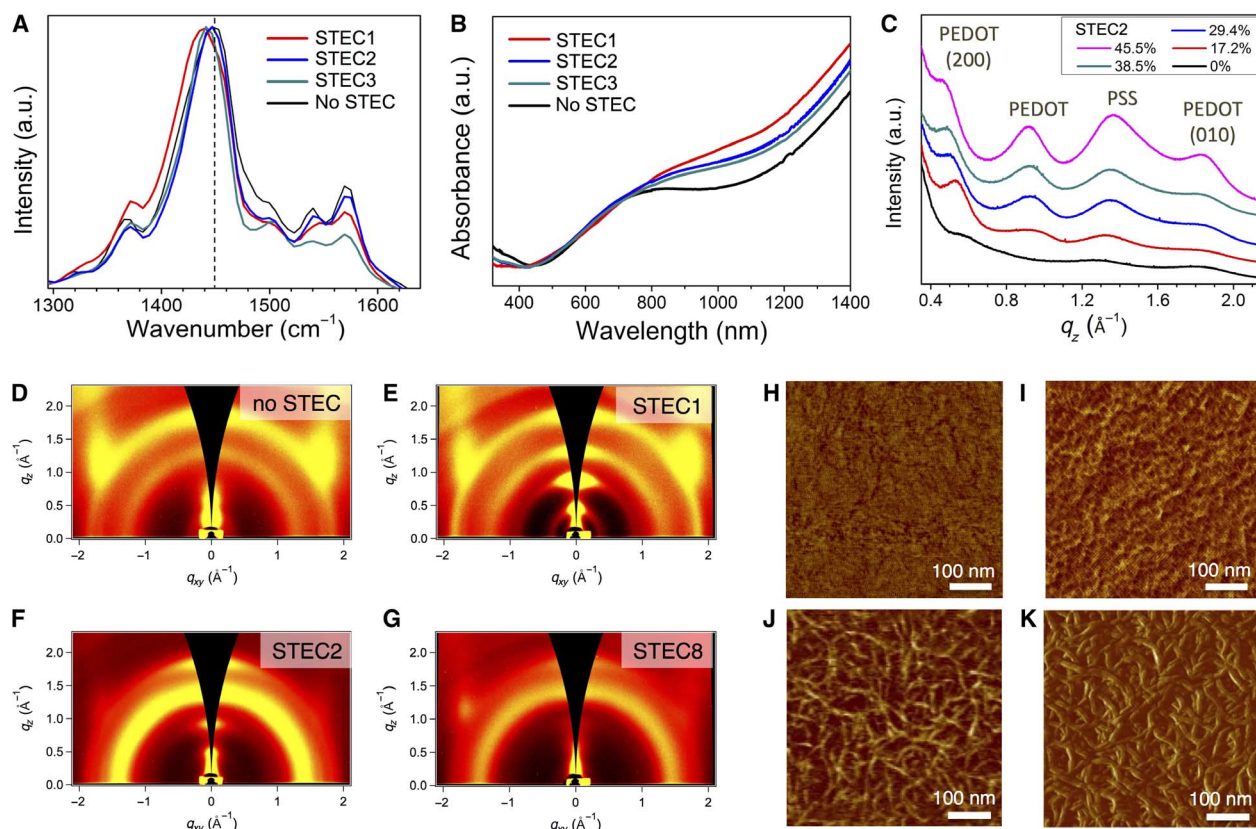


**Fig. 3. Chemical and crystallographic characterization of stretchable PEDOT.** (A) Raman spectra illustrating the  $C_{\alpha}=C_{\beta}$  peak position shift for the different films. The dashed line indicates the peak position for the PEDOT control film without any STEC. (B) UV-vis-NIR spectra showing the doping effect of STEC on PEDOT, as evidenced by increased absorption intensity from bipolaron delocalization at  $>1000\text{ nm}$ . (C) Near out-of-plane intensity plot of PEDOT:PSS films with various amounts of STEC2 additives extracted from GIWAXS patterns of PEDOT:PSS films with no STEC (D) and 45.5 wt % of STEC1 (E), STEC2 (F), and STEC8 (G) (see also section S3). For the standard PEDOT film without any STEC additives, three peaks were observed along  $q_z$ :  $q_z = 0.57\text{ \AA}^{-1}$  ( $d = 11.2\text{ \AA}$ ),  $1.33\text{ \AA}^{-1}$  ( $d = 4.9\text{ \AA}$ ), and  $1.87\text{ \AA}^{-1}$  ( $d = 3.4\text{ \AA}$ ), which can be indexed as PEDOT (200), PSS amorphous scattering, and PEDOT (010), respectively (40, 45). (H to K) AFM phase images of regular PEDOT:PSS (H) compared to PEDOT with high stretchability by incorporating STEC1 (I), STEC2 (J), and STEC3 (K).

in width in the PEDOT/STEC films compared to the pure PEDOT:PSS control (Fig. 3A). This indicates that a higher proportion of the benzoid moieties in PEDOT are converted to the quinoid structure from oxidative charge transfer doping, which results in a more planar backbone (25, 30, 31). This planarity may contribute to more efficient charge delocalization and a higher packing order (28). The charge delocalization effect is further confirmed by UV-vis-near-infrared (NIR) spectra (Fig. 3B) (32) because the ~800-nm peak became less well defined and a more intense free-carrier tail extending into the NIR was observed when STEC1, STEC2, and STEC3 were incorporated into PEDOT:PSS.

Grazing-incidence wide-angle x-ray scattering (GIWAXS) patterns indicate that the ordering in the semicrystalline PEDOT:PSS films was improved with the addition of STEC (Fig. 3, C to G, and fig. S5). Specifically, the (200) d-spacing increases with increased STEC contents in the films, which is accompanied by a slight decrease in d-spacing for the (010) peak (from 3.4 to 3.3 Å) (33–35). Meanwhile, with the addition of STEC, a new peak emerges at  $q_z = \sim 0.89 \text{ \AA}^{-1}$  ( $d = \sim 6.8 \text{ \AA}$ ), which was previously reported and assigned to PEDOT, but no definitive indexing was reported (33, 34). In addition, we observed this peak in the PEDOT:PF<sub>6</sub> system without PSS (fig. S6), further confirming that it arises from PEDOT scattering.

Combining the above evidences, we propose a schematic representation of the composition and morphology of the PEDOT/STEC films (Fig. 1D): The charge screening effect of the ionic STEC additives results in a morphological change to form more crystalline and more interconnected PEDOT nanofibrillar structures. Because the PEDOT phase becomes more crystalline with the addition of STEC, we suspect that it is likely that the STEC molecules mostly reside in the more disordered regions, which further softens the material. This gives rise to a nanofiber network embedded in a soft matrix, which is a desirable morphology for high stretchability. Such morphology is also advantageous for high conductivity because of the higher crystallinity of the PEDOT domains and the improved connectivity.

Films with the highest conductivity values were obtained with the above morphological improvement and an additional STEC washing of the films (Materials and Methods and figs. S15 to 17). X-ray photoelectron spectroscopy (XPS) sputtering experiments indicate that the surface of the as-spun PEDOT/STEC film has a higher PSS + STEC-to-PEDOT ratio than the interior of the film (Fig. 4B and fig. S17). Rinsing with an STEC aqueous solution after annealing removes the excess PSS from the film surface, leading to a thinner film with a higher PEDOT content, thus further improving the conductivity (figs. S16 and S17). Treating the films with water led to a similar effect in terms of conductivity enhancement, but STEC solutions are used here to minimize the loss of STEC plasticizers that are necessary for stretchability. The conductivity for PEDOT/STEC systems increased rapidly as the STEC concentration increased until ~45 wt % (Fig. 4A and figs. S15 to 17). It then remained nearly constant upon further addition. The highest conductivity values achieved were 2588, 3102, and 2544 S/cm at 71 wt % of STEC1, STEC2, and STEC3, respectively, versus 4 S/cm without these additives.

### Temperature dependence of conductivity

The chemical composition and morphology of materials have direct impact on the temperature dependence of the electrical conductivity, which provides insights into transport properties. Aiming at applications where highly stretchable materials are used as interconnects between different electronic components, possible temperature drifts have to be minimized. The temperature dependence of PEDOT thin films between 340 and 75 K were measured in a cryostat using a four-probe

dc current method (Fig. 4C). All samples exhibited reversible temperature dependence with low hysteresis, indicating high stability. An empirical relation has been used to extract the temperature resistance coefficients of first and second order (section S6). PEDOT with dimethyl sulfoxide as the additive exhibited a very high linear temperature resistance coefficient of about  $\alpha = 0.35\%/K$ , whereas PEDOT/STEC enhancers 1 and 2 showed much lower values of  $3.8 \times 10^{-7}$  and  $7.6 \times 10^{-3}\%/K$ , respectively.

A widely used model to describe the temperature behavior of disordered polymeric systems assumes that the charge transport is dominated by interchain hopping probability (36–38). The temperature dependence of these materials follows a non-Arrhenius quadratic expression originating from a Gaussian disorder and has been reported to describe systems with low charge carrier densities well. On the other hand, at high charge carrier densities, a universal Arrhenius-like temperature dependence has been observed for disordered conjugated polymers (39). Our stretchable PEDOT/STEC materials exhibited a clear temperature-activated behavior following the Arrhenius law (Fig. 4D). The activation energy extracted for PEDOT/STEC1 and PEDOT/STEC2 was found to be only about 3 and 4.1 meV, respectively. These values are much lower compared to typical PEDOT films, which have an activation energy of 15.2 meV. These results agree with the stronger free-carrier tails observed in UV-vis-NIR spectra (Fig. 3B), which suggest that STEC enhancers also act as “secondary” dopants for PEDOT. The doping effect increases the charge carrier density and shifts the Fermi level  $E_F$  above the equilibrium level  $E_q$ , which is represented by the maximum of the density of occupied states (39). The lowest activation energy of PEDOT/STEC1 remains in agreement with the highest room temperature conductivity and the lowest linear temperature resistance coefficient of  $3.8 \times 10^{-7}\%/K$ .

### Applications and patterning of stretchable PEDOT

Because the conductivity of the stretchable PEDOT remains well above 1000 S/cm even under 100% strain, only a thin layer is needed to achieve low resistance, rendering it a good transparent stretchable conductor. Figure 4E depicts the relationship between film transmittance and sheet resistance. A sheet resistance of 59 ohms/sq was obtained for a film with 96% transmittance (with substrate absorbance subtracted). This is among the highest values reported for PEDOT transparent electrodes, whereas none of the previously reported highly conductive ones were stretchable (25, 34, 40). The resistance decreased as the film thickness is increased, and it reached ~10 ohms/sq with a 75% film transmittance at 550 nm. The film with 96% transmittance has a figure of merit (FoM) of 142, which surpasses the previous highest value from spin-casted PEDOT films and transparent CNT electrodes (27, 34, 40, 41).

Larger patterns (that is, >500  $\mu\text{m}$ ) (Fig. 4F) can be readily obtained by screen printing or etching through a shadow mask and are stretchable when printed on an elastic substrate such as SEBS. Complex patterns with resolution down to 40  $\mu\text{m}$  can be obtained through inkjet printing (Fig. 4, G to I).

To demonstrate the application of stretchable PEDOT as interconnects, we used it to connect rigid LEDs (Fig. 5A). Negligible change in LED light intensity was observed even under high strain conditions, such as twisting while stretching or poking the interconnect with a sharp object (Fig. 5, B and C, and videos S1 and S2), due to the small change in resistance upon tensile strain.

One distinct advantage of an intrinsically stretchable conductor as interconnects for rigid-island matrices is that it can lead to a much higher surface filling ratio ( $f$ ) (42) for active devices (islands) compared to the wavy interconnects, where a large amount of space between the rigid islands needs to be reserved for the wavy metal ribbons (4, 6). To dem-

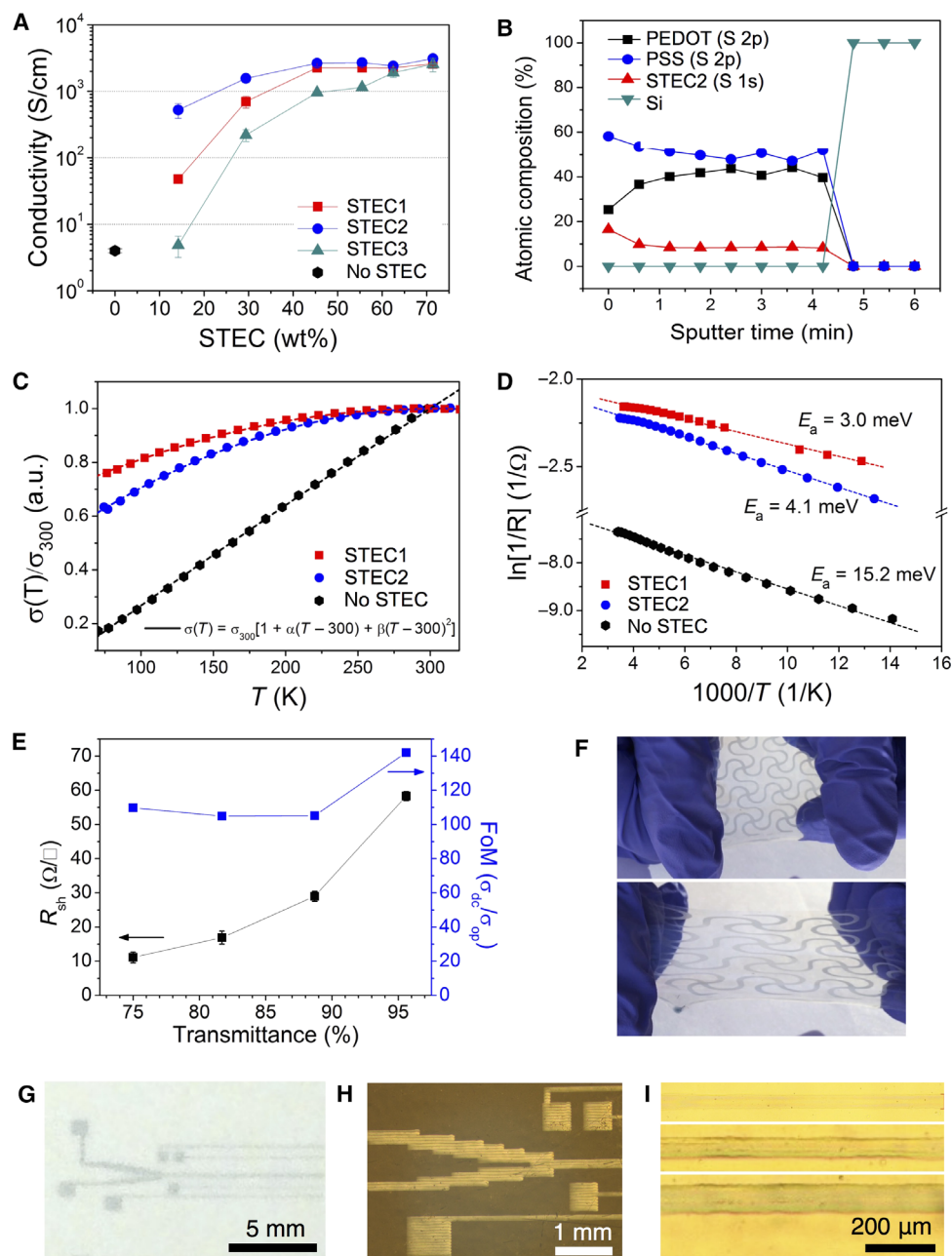


**Fig. 4. Electrical properties and patterning of the stretchable PEDOT/STEC (STEC content is 45.5 wt % for all).** (A) Conductivity of the PEDOT films via spin coating followed by various STEC aqueous solution treatments. (B) XPS  $C_{60}$  ion gun sputtering depth profile of a stretchable PEDOT/STEC film. (C) Temperature dependence of the conductivity and (D) Arrhenius fitting for conventional PEDOT compared to those with STEC additives. (E) Sheet resistance of the PEDOT/STEC1 films in relation to their transparency. Transmittance values are extracted at 550 nm. (F) Patterned PEDOT/STEC film on SEBS (top) and the film being stretched (bottom). The line width is 1 mm. (G and H) Photograph (G) and optical microscope image (H) showing micrometer-scale patterns produced by inkjet-printing the PEDOT/STEC. (I) Illustration of the control of feature size, with a line width as small as 40  $\mu m$  printed on a SEBS substrate.

onstrate the potential of PEDOT/STEC as interconnects in high-density circuits, we connected multiple rigid islands with field-effect transistor (FET) devices by lines of PEDOT (Fig. 5, F to H).

A rigid island-to-interconnect width of 1:1 ( $f = 50\%$ ) is typically required for wavy interconnects to reach stable performances under 100% strain (42). The actual length of the stretched interconnect is much longer than the spacing between rigid islands (for example, up to >12 times if straightened) (6). In our case, for unidirectional stretching, a rigid

island-to-interconnect ratio of as high as 5:1 ( $f = 78\%$ ) can still lead to identical transistor current and threshold voltage characteristics from 0 to 150% strain for the linear array (fig. S29), which inflicts >530% strain on the PEDOT region based on finite element simulations (Fig. 5, D and E).

To demonstrate the feasibility of multidimensional stretching, we fabricated  $3 \times 3$  arrays with  $f$  of 78% and uniformly stretched them in all directions. Figure S30 and table S2 show the transfer curves for the



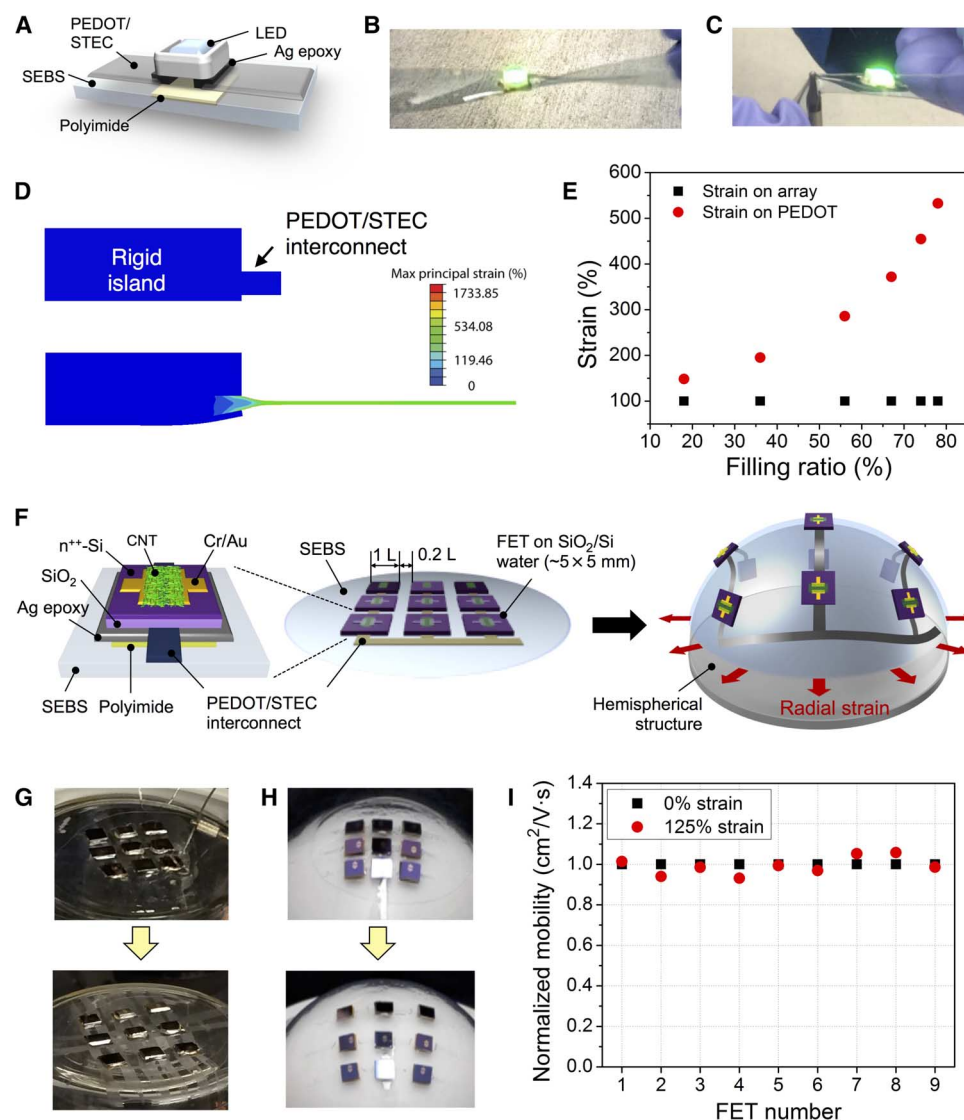


**Fig. 5. Stretchable PEDOT/STEC as interconnects for LED and FET devices.** (A) Schematic representation of an LED device bridged by PEDOT wires to the power source. (B and C) Photographs illustrating the minimal change in LED brightness as the device is stretched under twisting and poked with a sharp object, respectively. (D) Finite element simulation showing the cross-sectional strain distribution of the rigid-island arrays under 0% (top) and 100% (bottom) strains. (E) Plot summarizing the relationship between array density and strain on PEDOT interconnects when stretching the array to 100% from the simulation results. (F) Schematic diagram of the rigid-island FET array with stretchable PEDOT interconnects. (G and H) Photographs showing the FET array being stretched in all directions on a flat surface and spherical object, respectively. (I) Normalized mobility of individual transistors when the array is stretched to different strains.

nine transistors under 0 and 125% strains for overall device structure. The mobility variation for all the transistors is within  $\pm 10\%$  (Fig. 5I). This strain is well beyond the 100% strain requirement for wearable and epidermal electronics, illustrating the excellent stretchability and the stable electrical performances of the PEDOT interconnects under strain. This array is especially suitable for stable performance on curved objects (Fig. 5H, fig. S31, and video S3).

## DISCUSSION

We have demonstrated a highly stretchable and conductive PEDOT polymer by incorporating ionic additive–assisted STEC enhancers that result in a morphology that is beneficial for both high stretchability and conductivity. A further boost in conductivity is achieved through a

proper selection of anions. The resulting materials show record-high stretchability and conductivity, the coexistence of which is rare for conducting polymers. High-density FET arrays connected using the stretchable PEDOT films show stable performance under  $>100\%$  strain. This material synergistically combines high electrical conductivity, exceptional mechanical ductility, and patternability by printing, thus opening many new avenues toward next-generation wearable and epidermal electronics and bioelectronics.

## MATERIALS AND METHODS

### Material preparation

PEDOT:PSS (PH1000) was obtained from Clevios, and the STEC ionic additives were obtained from Sigma-Aldrich and Santa Cruz Biotechnology,

Inc. SEBS with 20% styrene content (Tuftec H1052) was supplied by AK Elastomer. HiPco single-walled CNT (SWCNT) was sorted via a previously reported method (43) using poly(3-dodecylthiophene-2,5-diyl) (P3DDT) to obtain semiconducting SWCNT for transistor fabrication.

In a typical experiment, STEC of 10 to 71 wt % was added to the PEDOT:PSS aqueous dispersion (1.1 to 1.3 wt %) and stirred vigorously for 15 min. Thick films were acquired by drying the mixture overnight in a Teflon mold and then annealing at 130°C for 15 min. Thin films were processed onto glass, SiO<sub>2</sub>/Si, or SEBS substrates by spin coating at 1000 rpm for 1 min under ambient conditions, followed by a 10-min annealing at 130°C. A postdeposition washing step was then carried out by dropping an aqueous solution containing 10 mg/ml of the corresponding STEC on the PEDOT films, waiting for 1 min, and removing the liquid by spinning the samples at 3000 rpm for 1 min. Glass or SiO<sub>2</sub>/Si was treated with oxygen plasma at 150 W for 30 s, and SEBS was treated with UV ozone for 30 min or with oxygen plasma for 10 s (150 W) before PEDOT deposition via spin coating (1000 rpm for 1 min, followed by annealing at 70°C for 30 min). The SEBS substrates were prepared from a toluene solution (200 mg/ml) casted onto a glass slide.

### Electrical property

Conductivity measurements were carried out using a four-point geometry. Electrodes were deposited by applying silver paste or eGaIn or by evaporating gold. A minimum of three to five measurements were obtained for an average value. Low temperature-dependent measurements were performed in a LakeShore cryostat under 10<sup>−5</sup> mbar vacuum. A bottom gold contact geometry was used to ensure stable electrical contacts under thermal cycling. A slow cooling and heating rate of about 1.4 K/min assured the stabilization at each temperature.

### Mixed ion-electron conductivity

Mixed ion-electron conductivity was studied using impedance measurements. The PEDOT films with STEC enhancers were cut into round tablets (diameter, 3.5 mm; thickness, ca. 100 μm). Two glassy carbon electrodes (diameter, 3 mm) were used to sandwich the tablet to form an electrical contact for the impedance measurement. The impedance data as functions of frequency were acquired by a Bio-Logic VSP-300 workstation with a sine wave signal amplitude of 10 mV. Resistances from the ionic versus electronic components were calculated using previously reported procedures (44).

### Mechanical property

Mechanical properties of freestanding films around 200 μm in thickness were studied using Instron 5565 with a 100-N loading cell using dumbbell film geometry. The storage, loss moduli, and stress relaxation tests were carried out on a dynamic mechanical analysis (TA Instruments Q800).

### Morphological and chemical characterization

Microscopy was performed on a FEI XL30 Sirion scanning electron microscope. AFM images were recorded in tapping mode using a Veeco Multimode AFM. UV-vis-NIR spectra were collected on an Agilent Cary 6000i model. Dynamic light scattering experiments were carried out using 100-fold diluted PEDOT/STEC dispersions on a Brookhaven Instrument 90. XPS was performed on a PHI VersaProbe Scanning XPS Microprobe. Sputtering was carried out at 10 kV and 20 mA with a C<sub>60</sub> ion sputtering gun to preserve the chemical information in the polymer films. Film thickness values were measured using a contact probe Dektak 150 profilometer and averaged from a minimum of three areas.

### Grazing-incidence x-ray scattering

GIWAXS measurements were carried out at the Stanford Synchrotron Radiation Lightsource at beamline 11-3, with a photon energy of 12.735 KeV and a sample-to-detector distance of 320 mm. The incident angle was fixed at 0.14° to probe the entire film with reduced substrate scattering.

### Patterning

Patterned films [feature size, >500 μm (such as for the LED or FET arrays)] were obtained by repeating the spin coating and washing steps three times for PEDOT on SEBS, followed by oxygen plasma etching (150 W for 5 to 10 min) through a shadow mask until the exposed PEDOT films were completely removed.

Micrometer-sized patterns of the stretchable PEDOT/STEC were achieved through inkjet printing using a fourfold diluted dispersion. The dispersion was passed through a glass fiber syringe filter with a pore size of 0.7 μm and degassed for a few minutes to remove trapped air bubbles before it was loaded into a cartridge. A Dimatix Fujifilm DMP 2800 inkjet printer with 10-pl drop volume cartridges was used to print this ink on different substrates, such as SiO<sub>2</sub>/Si, SEBS, or photo paper. The optimal printing parameters for plasma-treated SEBS substrate (150 W for 10 s) were as follows: drop-to-drop spacing of 30 μm; a jet speed and a frequency of 5 m/s and 1.5 kHz, respectively; a cartridge temperature of 28°C, and a substrate temperature of 30°C.

### Stretchable rigid-island transistor arrays

Transistors on rigid Si islands in our arrays were fabricated by first patterning the Cr/Au (5/40 nm) source and drain electrodes through a shadow mask on a SiO<sub>2</sub>/n<sup>++</sup>-Si wafer (Si and SiO<sub>2</sub> serve as the back gate and dielectric layer, respectively). Each FET device has a channel width of 1000 μm and a channel length of 200 μm. The sorted SWCNT dispersion (0.7 ml) (43) was spin-coated on the patterned substrates (2 in × 2 in) at 2000 rpm for 90 s. The sample was then soaked in toluene at 90°C for 30 min to remove the P3DDT, dried with nitrogen flow, and annealed at 120°C for 20 min under ambient conditions. Polydimethylsiloxane shadow masks were aligned on the devices to protect the active device areas. The SWCNTs between devices were then etched away by oxygen plasma (150 W for 10 min). Single rigid-island devices were obtained by dividing the whole piece into 5-cm × 5-cm chips along the CNT-free spaces. The 3 × 3 stretchable organic transistor active matrices were fabricated by immobilizing the individual islands using silver epoxy onto a SEBS substrate and linked together using patterned PEDOT/STEC1, creating a common back gate (Fig. 5F). Under ambient conditions, the transistor performance was characterized using a Keithley 4200 SC semiconductor analyzer under different strains for each rigid island while applying common gate voltages through the PEDOT interconnects.

### Finite element simulation

Finite element analysis for simulating the strain distributions in the FET arrays was carried out using the software Abaqus.

### SUPPLEMENTARY MATERIALS

Supplementary material for this article is available at <http://advances.sciencemag.org/cgi/content/full/3/3/e1602076/DC1>

- section S1. Selection of STEC enhancers
- section S2. Mechanical characterization of bulk freestanding films
- section S3. Effect of STEC on PEDOT:PSS
- section S4. Morphology of PEDOT/STEC film interior
- section S5. Microscopy study of the effect of tensile strain on PEDOT/STEC films
- section S6. Electrical properties of PEDOT/STEC films



section S7. Composition of PEDOT/STEC films  
 section S8. Low-temperature measurements  
 section S9. FoM for transparent conductors  
 section S10. Testing geometry for PEDOT films under tensile strain  
 section S11. Polarized UV-vis-NIR spectra for PEDOT films under tensile strain  
 section S12. Cycling stability and morphological change of PEDOT with STEC additives  
 section S13. Mixed ion-electron conductivity  
 section S14. PEDOT/STEC as interconnects for FET arrays  
 table S1. Summary of STEC structures and their effects on the electrical and mechanical properties of freestanding PEDOT:PSS films (thickness range, 150 to 200  $\mu\text{m}$ ) with 45.5 wt % of STEC.  
 table S2. Summary of mobility and threshold voltage shift for the  $3 \times 3$  transistor arrays under 0 and 125% strain.  
 fig. S1. Plot summarizing the conductivity, maximum tensile strain, and Young's modulus for freestanding PEDOT:PSS films ( $\sim 150 \mu\text{m}$  in thickness) with all additives investigated in this paper.  
 fig. S2. Mechanical characterization of bulk freestanding films.  
 fig. S3. Mechanism behind STEC-induced morphology change for PEDOT:PSS films.  
 fig. S4. AFM phase images of PEDOT with various additives.  
 fig. S5. GIWAXS analyses of PEDOT films.  
 fig. S6. Diffraction data for PSS and insoluble PEDOT control samples.  
 fig. S7. Plasticizing effect of STEC on PEDOT and NaPSS individually.  
 fig. S8. SEM characterization of the cross section of a stretchable PEDOT film.  
 fig. S9. Optical microscope images of a PEDOT/STEC1 film supported on a SEBS substrate under various strains.  
 fig. S10. Optical microscope images of a PEDOT/STEC1 film supported on a SEBS substrate after being stretched to various strains and returned to its original length.  
 fig. S11. Surface profile analyses of PEDOT films after stretching.  
 fig. S12. Optical microscope images of a PEDOT/STEC1 film upon unloading from 100% strain.  
 fig. S13. Optical microscope images of a PEDOT/STEC2 film held under various tensile strains.  
 fig. S14. Optical microscope images of a PEDOT/STEC2 film upon stretching to various tensile strains.  
 fig. S15. Conductivity values of PEDOT/STEC films processed under different conditions.  
 fig. S16. Conductivity of PEDOT/STEC films with various STEC weight % before and after further STEC solution treatment.  
 fig. S17. Effect of further doping using STEC solution on spin-coated films.  
 fig. S18. Chemical composition of PEDOT/STEC films.  
 fig. S19. Temperature-dependent conductivity and first- and second-order temperature coefficients for PEDOT films.  
 fig. S20. Arrhenius plots for temperature dependent conductivity.  
 fig. S21. Schematic diagrams of tensile testing and conductivity measurement geometries.  
 fig. S22. Tension-induced chain-alignment behavior of PEDOT/STEC films.  
 fig. S23. XPS analysis of film surfaces under 0% versus 100% strain, after returning from 100% to 0% strain, and after 1000 stretching cycles to 100% strain.  
 fig. S24. Cycling stability of PEDOT/STEC1 films.  
 fig. S25. Cycling stability of PEDOT/STEC2 films.  
 fig. S26. Mixed ion-electron conductivity measurements.  
 fig. S27. Schematic showing the cross-sectional view of a linear rigid-island array connected with stretchable PEDOT.  
 fig. S28. Schematic diagrams illustrating strain calculation for rigid-island devices.  
 fig. S29. Schematic and transfer characteristics for a  $3 \times 1$  FET array.  
 fig. S30. Schematic and transfer characteristics for a  $3 \times 3$  FET array.  
 fig. S31. A  $3 \times 3$  FET array being stretched on a spherical object.  
 video S1. A stretchable LED device poked with a sharp object.  
 video S2. Twisting and stretching of a stretchable LED device.  
 video S3. A  $3 \times 3$  FET array stretched on a spherical object.

## REFERENCES AND NOTES

1. S. Wagner, S. Bauer, Materials for stretchable electronics. *MRS Bull.* **37**, 207–213 (2012).
2. M. L. Hammock, A. Chortos, B. C.-K. Tee, J. B.-H. Tok, Z. Bao, The evolution of electronic skin (E-skin): A brief history, design considerations, and recent progress. *Adv. Mater.* **25**, 5997–6038 (2013).
3. I. Jung, J. Xiao, V. Malyarchuk, C. Lu, M. Li, Z. Liu, J. Yoon, Y. Huang, J. A. Rogers, Dynamically tunable hemispherical electronic eye camera system with adjustable zoom capability. *Proc. Natl. Acad. Sci. U.S.A.* **108**, 1788–1793 (2011).
4. D.-H. Kim, J.-H. Ahn, W. Mook Choi, H.-S. Kim, T.-H. Kim, J. Song, Y. Y. Huang, Z. Liu, C. Lu, J. A. Rogers, Stretchable and foldable silicon integrated circuits. *Science* **320**, 507–511 (2008).
5. D. J. Lipomi, M. Vosgueritchian, B. C. Tee, S. L. Hellstrom, J. A. Lee, C. H. Fox, Z. Bao, Skin-like pressure and strain sensors based on transparent elastic films of carbon nanotubes. *Nat. Nanotechnol.* **6**, 788–792 (2011).
6. X. Hu, P. Krull, B. de Graff, K. Dowling, J. A. Rogers, W. J. Arora, Stretchable inorganic-semiconductor electronic systems. *Adv. Mater.* **23**, 2933–2936 (2011).
7. T. Sekitani, Y. Noguchi, K. Hata, T. Fukushima, T. Aida, T. Someya, A rubberlike stretchable active matrix using elastic conductors. *Science* **321**, 1468–1472 (2008).
8. S. Yao, Y. Zhu, Nanomaterial-enabled stretchable conductors: Strategies, materials and devices. *Adv. Mater.* **27**, 1480–1511 (2015).
9. D.-H. Kim, J. A. Rogers, Stretchable electronics: Materials strategies and devices. *Adv. Mater.* **20**, 4887–4892 (2008).
10. C. Yan, P. S. Lee, Stretchable energy storage and conversion devices. *Small* **10**, 3443–3460 (2014).
11. T. C. Shyu, P. F. Damasceno, P. M. Dodd, A. Lamoureux, L. Xu, M. Shlian, M. Shtein, S. C. Glotzer, N. A. Kotov, A kirigami approach to engineering elasticity in nanocomposites through patterned defects. *Nat. Mater.* **14**, 785–789 (2015).
12. H. Vandeparre, Q. Liu, I. R. Mineev, Z. Suo, S. P. Lacour, Localization of folds and cracks in thin metal films coated on flexible elastomer foams. *Adv. Mater.* **25**, 3117–3121 (2013).
13. A. Chortos, J. Lim, J. W. F. To, M. Vosgueritchian, T. J. Dusseault, T.-H. Kim, S. Hwang, Z. Bao, Highly stretchable transistors using a microcracked organic semiconductor. *Adv. Mater.* **26**, 4253–4259 (2014).
14. T. S. Hansen, K. West, O. Hassager, N. B. Larsen, Highly stretchable and conductive polymer material made from poly(3,4-ethylenedioxythiophene) and polyurethane elastomers. *Adv. Funct. Mater.* **17**, 3069–3073 (2007).
15. K.-Y. Chun, Y. Oh, J. Rho, J.-H. Ahn, Y.-J. Kim, H. Ryeol Choi, S. Baik, Highly conductive, printable and stretchable composite films of carbon nanotubes and silver. *Nat. Nanotechnol.* **5**, 853–857 (2010).
16. N. Matsuhisa, M. Kaltenbrunner, T. Yokota, H. Jinno, K. Kuribara, T. Sekitani, T. Someya, Printable elastic conductors with a high conductivity for electronic textile applications. *Nat. Commun.* **6**, 7461 (2015).
17. K. Tybrandt, J. Vörös, Fast and efficient fabrication of intrinsically stretchable multilayer circuit boards by wax pattern assisted filtration. *Small* **12**, 180–184 (2016).
18. Y. Kim, J. Zhu, B. Yeom, M. Di Prima, X. Su, J.-G. Kim, S. J. Yoo, C. Uher, N. A. Kotov, Stretchable nanoparticle conductors with self-organized conductive pathways. *Nature* **500**, 59–63 (2013).
19. S. Savagatrup, E. Chan, S. M. Renteria-García, A. D. Printz, A. V. Zaretski, T. F. O'Connor, D. Rodriguez, E. Valle, D. J. Lipomi, Plasticization of PEDOT:PSS by common additives for mechanically robust organic solar cells and wearable sensors. *Adv. Funct. Mater.* **25**, 427–436 (2015).
20. D. J. Lipomi, J. A. Lee, M. Vosgueritchian, B. C.-K. Tee, J. A. Bolander, Z. Bao, Electronic properties of transparent conductive films of PEDOT:PSS on stretchable substrates. *Chem. Mater.* **24**, 373–382 (2012).
21. J. Y. Oh, S. Kim, H.-K. Baik, U. Jeong, Conducting polymer dough for deformable electronics. *Adv. Mater.* **28**, 4455–4461 (2016).
22. S. Savagatrup, A. D. Printz, T. F. O'Connor, A. V. Zaretski, D. J. Lipomi, Molecularly stretchable electronics. *Chem. Mater.* **26**, 3028–3041 (2014).
23. R. J. Young, P. A. Lovell, *Introduction to Polymers* (CRC Press, ed. 3, 2011).
24. D. Liu, R. Osuna Orozco, T. Wang, Deviations of the glass transition temperature in amorphous conjugated polymer thin films. *Phys. Rev. E* **88**, 022601 (2013).
25. J. Ouyang, "Secondary doping" methods to significantly enhance the conductivity of PEDOT:PSS for its application as transparent electrode of optoelectronic devices. *Displays* **34**, 423–436 (2013).
26. A. Elschner, S. Kirchmeyer, W. Lovenich, U. Merker, K. Reuter, *PEDOT: Principles and Applications of an Intrinsically Conductive Polymer* (CRC Press, ed. 1, 2010).
27. Y. Hyun Kim, C. Sachse, M. L. Machala, C. May, L. Müller-Meskamp, K. Leo, Highly conductive PEDOT:PSS electrode with optimized solvent and thermal post-treatment for ITO-free organic solar cells. *Adv. Funct. Mater.* **21**, 1076–1081 (2011).
28. J. Ouyang, C.-W. Chu, F.-C. Chen, Q. Xu, Y. Yang, High-conductivity poly(3,4-ethylenedioxythiophene):poly(styrene sulfonate) film and its application in polymer optoelectronic devices. *Adv. Funct. Mater.* **15**, 203–208 (2005).
29. Y. Xia, J. Ouyang, Salt-induced charge screening and significant conductivity enhancement of conducting poly(3,4-ethylenedioxythiophene):poly(styrenesulfonate). *Macromolecules* **42**, 4141–4147 (2009).
30. S. Garreau, J. L. Duval, G. Louarn, Spectroelectrochemical studies of poly(3,4-ethylenedioxythiophene) in aqueous medium. *Synth. Met.* **125**, 325–329 (2001).
31. S. Garreau, G. Louarn, J. P. Buisson, G. Froyer, S. Lefrant, In situ spectroelectrochemical Raman studies of poly(3,4-ethylenedioxythiophene) (PEDT). *Macromolecules* **32**, 6807–6812 (1999).
32. M. Lapkowski, A. Proń, Electrochemical oxidation of poly(3,4-ethylenedioxythiophene)—"In situ" conductivity and spectroscopic investigations. *Synth. Met.* **110**, 79–83 (2000).
33. N. Kim, B. Hoon Lee, D. Choi, G. Kim, H. Kim, J.-R. Kim, J. Lee, Y. H. Kahng, K. Lee, Role of interchain coupling in the metallic state of conducting polymers. *Phys. Rev. Lett.* **109**, 106405 (2012).
34. N. Kim, S. Kee, S. Ho Lee, B. H. Lee, Y. H. Kahng, Y.-R. Jo, B.-J. Kim, K. Lee, Highly conductive PEDOT:PSS nanofibrils induced by solution-processed crystallization. *Adv. Mater.* **26**, 2268–2272 (2014).
35. C. M. Alumbiny, F. Liu, T. P. Russell, A. Hexemer, C. Wang, P. Müller-Buschbaum, The crystallization of PEDOT:PSS polymeric electrodes probed in situ during printing. *Adv. Mater.* **27**, 3391–3397 (2015).

36. H. Bässler, Charge transport in disordered organic photoconductors a Monte Carlo simulation study. *Phys. Status Solidi B* **175**, 15–56 (1993).
37. S. D. Baranovskii, H. Cordes, F. Hensel, G. Leising, Charge-carrier transport in disordered organic solids. *Phys. Rev. B* **62**, 7934–7938 (2000).
38. R. Coehoorn, W. F. Pasveer, P. A. Bobbert, M. A. J. Michels, Charge-carrier concentration dependence of the hopping mobility in organic materials with Gaussian disorder. *Phys. Rev. B* **72**, 155206 (2005).
39. N. I. Craciun, J. Wildeman, P. W. M. Blom, Universal Arrhenius temperature activated charge transport in diodes from disordered organic semiconductors. *Phys. Rev. Lett.* **100**, 056601 (2008).
40. B. J. Worfolk, S. C. Andrews, S. Park, J. Reinspach, N. Liu, M. F. Toney, S. C. B. Mannsfeld, Z. Bao, Ultrahigh electrical conductivity in solution-sheared polymeric transparent films. *Proc. Natl. Acad. Sci. U.S.A.* **112**, 14138–14143 (2015).
41. B. Dan, G. C. Irvin, M. Pasquali, Continuous and scalable fabrication of transparent conducting carbon nanotube films. *ACS Nano* **3**, 835–843 (2009).
42. H. R. Fu, S. Xu, R. X. Xu, J. Q. Jiang, Y. H. Zhang, J. A. Rogers, Y. G. Huang, Lateral buckling and mechanical stretchability of fractal interconnects partially bonded onto an elastomeric substrate. *Appl. Phys. Lett.* **106**, 091902 (2015).
43. H. Wang, B. Cobb, A. van Breemen, G. Gelinck, Z. Bao, Highly stable carbon nanotube top-gate transistors with tunable threshold voltage. *Adv. Mater.* **26**, 4588–4593 (2014).
44. C. Wang, J. Hong, Ionic/electronic conducting characteristics of LiFePO<sub>4</sub> cathode materials: The determining factors for high rate performance. *Electrochem. Solid State Lett.* **10**, A65–A69 (2007).
45. K. E. Aasmundtveit, E. J. Samuelsen, O. Inganäs, L. A. A. Pettersson, T. Johansson, S. Ferrer, Structural aspects of electrochemical doping and dedoping of poly(3,4-ethylenedioxythiophene). *Synth. Met.* **113**, 93–97 (2000).

**Acknowledgments:** We thank H.-H. Chou for helpful discussions and M. Nalamachu for assistance in preparation of LED devices. **Funding:** This work was supported by Samsung Electronics

and Air Force Office of Scientific Research (grant no. FA9550-15-1-0106). R.P. acknowledges support from the Marie Curie Cofund, Beatriu de Pinós fellowship (Agència de Gestió d'Ajuts Universitaris i de Recerca, 2014 BP-A 00094). F.L. and F.M.-L. thank the Swiss National Science Foundation for an Early Mobility Postdoc grant. N.I.R. thanks the Stanford Graduate Fellowship and the NSF Graduate Research Fellowship Program. C.L. gratefully acknowledges additional support of the NSF through grant CMMI-1553638. Use of the Stanford Synchrotron Radiation Lightsource, SLAC National Accelerator Laboratory, was supported by the U.S. Department of Energy, Office of Science, Office of Basic Energy Sciences under contract no. DE-AC02-76SF00515. **Author contributions:** Y.W. and Z.B. conceived the concept. Y.W. carried out material preparation, characterization, and measurements. C.Z. fabricated FET arrays. R.P. performed low-temperature measurements. H.Y. performed GIWAXS data collection and analysis. L.J. simulated the strain distribution in rigid-island arrays. S.C. carried out XPS measurements. F.M.-L. inkjet-printed micrometer-sized patterns. F.L. and Y.W. performed AFM analyses. J.L. carried out mixed ion-electron conductivity measurements. N.I.R. helped with material preparation. Z.C. aided with the experimental design. J.W.C., C.L., M.F.T., B.M., and Z.B. supervised the project. All authors participated in data analysis and manuscript preparation. **Competing interests:** Y.W. and Z.B. applied for a patent related to the work (US 62/279,561) through Stanford University. All other authors declare that they have no competing interests. **Data and materials availability:** All data needed to evaluate the conclusions in the paper are present in the paper and/or the Supplementary Materials. Additional data related to this paper may be requested from the authors.

Submitted 30 August 2016

Accepted 16 February 2017

Published 10 March 2017

10.1126/sciadv.1602076

**Citation:** Y. Wang, C. Zhu, R. Pfattner, H. Yan, L. Jin, S. Chen, F. Molina-Lopez, F. Lissel, J. Liu, N. I. Rabiah, Z. Chen, J. W. Chung, C. Linder, M. F. Toney, B. Murmann, Z. Bao, A highly stretchable, transparent, and conductive polymer. *Sci. Adv.* **3**, e1602076 (2017).

This article is published under a Creative Commons license. The specific license under which this article is published is noted on the first page.

For articles published under [CC BY](#) licenses, you may freely distribute, adapt, or reuse the article, including for commercial purposes, provided you give proper attribution.

For articles published under [CC BY-NC](#) licenses, you may distribute, adapt, or reuse the article for non-commercial purposes. Commercial use requires prior permission from the American Association for the Advancement of Science (AAAS). You may request permission by clicking [here](#).

**The following resources related to this article are available online at <http://advances.sciencemag.org>. (This information is current as of April 2, 2017):**

**Updated information and services**, including high-resolution figures, can be found in the online version of this article at:

<http://advances.sciencemag.org/content/3/3/e1602076.full>

**Supporting Online Material** can be found at:

<http://advances.sciencemag.org/content/suppl/2017/03/06/3.3.e1602076.DC1>

This article **cites 43 articles**, 4 of which you can access for free at:

<http://advances.sciencemag.org/content/3/3/e1602076#BIBL>

Science Advances (ISSN 2375-2548) publishes new articles weekly. The journal is published by the American Association for the Advancement of Science (AAAS), 1200 New York Avenue NW, Washington, DC 20005. Copyright is held by the Authors unless stated otherwise. AAAS is the exclusive licensee. The title Science Advances is a registered trademark of AAAS